

LETTER TO THE EDITOR

A HARPS view on K2-3[★]

J.M. Almenara^{1,2}, N. Astudillo-Defru^{1,2}, X. Bonfils^{1,2}, T. Forveille^{1,2}, A. Santerne³, S. Albrecht⁴, S.C.C. Barros⁵, F. Bouchy⁵, X. Delfosse^{1,2}, O. Demangeon⁵, R.F. Díaz⁶, G. Hébrard^{7,8}, M. Mayor⁶, V. Neves⁹, P. Rojo¹⁰, N.C. Santos^{3,11}, and A. Wünsche^{1,2}

¹ Univ. Grenoble Alpes, IPAG, F-38000 Grenoble, France

² CNRS, IPAG, F-38000 Grenoble, France

³ Instituto de Astrofísica e Ciências do Espaço, Universidade do Porto, CAUP, Rua das Estrelas, PT4150-762 Porto, Portugal

⁴ Stellar Astrophysics Centre, Department of Physics and Astronomy, Aarhus University, Ny Munkegade 120, DK-8000 Aarhus C, Denmark

⁵ Aix Marseille Université, CNRS, LAM (Laboratoire d'Astrophysique de Marseille) UMR 7326, 13388, Marseille, France

⁶ Observatoire Astronomique de l'Université de Genève, 51 chemin des Maillettes, 1290 Versoix, Switzerland

⁷ Observatoire de Haute Provence, 04670 Saint Michel l'Observatoire, France

⁸ Institut d'Astrophysique de Paris, UMR7095 CNRS, Université Pierre & Marie Curie, 98bis boulevard Arago, 75014 Paris, France

⁹ Departamento de Física, Universidade Federal do Rio Grande do Norte, 59072-970 Natal, RN, Brazil

¹⁰ Departamento de Astronomía, Universidad de Chile, Santiago, Chile

¹¹ Departamento de Física e Astronomia, Faculdade de Ciências, Universidade do Porto, Rua do Campo Alegre 687, PT4169-007 Porto, Portugal

ABSTRACT

K2 space observations recently found that three super-Earths transit the nearby M dwarf K2-3. The apparent brightness and the small physical radius of their host star rank these planets amongst the most favourable for follow-up characterisations. The outer planet orbits close to the inner edge of the habitable zone and might become one of the first exoplanets searched for biomarkers using transmission spectroscopy. We used the HARPS velocimeter to measure the mass of the planets. The mass of planet *b* is $8.4 \pm 2.1 M_{\oplus}$, while our determination of those planets *c* and *d* are affected by the stellar activity. With a density of $4.32^{+2.0}_{-0.76} \text{ g cm}^{-3}$, planet *b* is probably mostly rocky, but it could contain up to 50% water.

Key words. stars: individual: K2-3 – stars: planetary systems – stars: late-type – technique: radial-velocity – techniques: photometry

1. Introduction

Crossfield et al. (2015) have recently reported from *K2* (Howell et al. 2014) observations that the star K2-3 (2MASS 11292037-0127173, EPIC 201367065) hosts a planetary system with three transiting super-Earths. The star is an inactive M0 dwarf ($T_{\text{eff}} = 3900 \pm 190 \text{ K}$, $[\text{Fe}/\text{H}] = -0.32 \pm 0.13 \text{ dex}$), and it is bright enough to be amenable to transit spectroscopy. With a radius of $1.5 R_{\oplus}$, Planet *d* orbits close to the inner edge of the system's habitable zone. The mass of the planets has not been measured to date.

To constrain those masses, we monitored the radial velocity of K2-3 with the HARPS velocimeter (Mayor et al. 2003). We jointly analysed these new velocities and the *K2* photometry through n-body integrations to obtain the mass of planets. Combined with the planet sizes, this constrains their mean densities and bulk compositions and

helps explore the rocky–gaseous transition in the super-Earth regime.

2. Observations

2.1. *K2* light curve

The *K2* mission observed K2-3 during its Campaign 1 (Summer 2014) in long cadence mode¹. We downloaded the pixel data from the Mikulski Archive for Space Telescopes (MAST)² and used a modified version of the CoRoT imagerie pipeline (Barros et al. 2014) to extract a light curve. The procedure first determines the circular synthetic aperture that maximises the photometric signal-to-noise ratio on the mean image. For each image, it then computes a modified moment method centroid (Stone 1989) and recentres a heavily oversampled version of the image on the centroid before extracting the flux inside the pre-determined aperture. The degraded pointing stability of the *K2* mis-

[★] Based on observations made with the HARPS instrument on the ESO 3.6 m telescope under the program ID 191-C0873 at Cerro La Silla (Chile).

¹ <http://archive.stsci.edu/k2/>

² http://archive.stsci.edu/kepler/data_search/search.php

sion couples with pixel sensitivity variations to introduce position-dependent systematics in the raw light curves. To correct for this flux dependence with position, we used a procedure inspired by Vanderburg & Johnson (2014). The light curve was divided into seven equal duration segments, and for each segment we performed a 1D decorrelation as described in Vanderburg (2014). We found that a 21-pixel photometric aperture results in the best photometric precision of the final light curve with a 204 ppm mean RMS. The 80-day light curve contains eight transits of Planet *b*, four of Planet *c*, and two of Planet *d*. We only modelled the light curve around those transits, after normalising it with a parabolic fit to its out-of-transit part. To account for the 29.4 minutes integration time of the long cadence data, we oversampled the model light curve by a factor of 20 and then binned it to the cadence of the data points.

2.2. HARPS radial velocities

We obtained differential radial velocities (RVs) with HARPS, the ESO velocimeter installed at the focus of the 3.6m telescope at La Silla Observatory (Mayor et al. 2003; Pepe et al. 2003). We chose not to use simultaneous wavelength calibration and to instead rely on the $<1 \text{ ms}^{-1}$ stability of the HARPS spectrograph, since we expected significantly larger photon noise errors. We tried to secure two 1800 s observations per night and collected 66 spectra over a timespan of 103 days.

For an optimal extraction of the velocity signal, we used all recorded spectra (already extracted and wavelength-calibrated by the online pipeline, Lovis & Pepe 2007) to build stellar templates. We shifted each spectrum by its barycentric correction and co-added those shifted spectra into higher S/N templates after carefully masking the telluric absorption lines.

When using such a small set of relatively noisy spectra, we would bias the velocity if we included the spectrum analysed for Doppler shift in the template that it is matched against, since their common noise pattern will contribute to the match. To avoid this bias, we built one template for each spectrum by co-adding all spectra but the spectrum itself.

We then computed the RV shifts that minimise the χ^2 difference between the individual spectra and their templates (e.g. Zucker & Mazeh 2006; Anglada-Escudé & Butler 2012; Astudillo-Defru et al. 2014). The 66 resulting velocities, listed in Table A.1, have a 4.9 ms^{-1} dispersion for a median uncertainty of 2.9 ms^{-1} (compared with 7.1 ms^{-1} and 4.3 ms^{-1} for the velocities measured by the HARPS pipeline). Although the orbital periods are known from the photometry and do not need to be identified from the RVs alone, Fig. A.1 shows their periodogram for illustration.

2.3. Stellar activity

The HARPS spectral range includes both $H\alpha$ and the Ca II H&K lines, which are good tracers of stellar activity. While $H\alpha$ is a pure absorption line in K2-3 and does not measurably vary, its Ca II lines, as for all M dwarfs, do have emission cores. We quantify the Ca II H&K flux through the S index (Vaughan et al. 1978) and find that it varies by 30% on a timescale that is longer than the ten-day period of Planet *b*. K2-3 has a lower average S index than

Gl 846, an M0.5V star with a ~ 10.6 -day rotation period (Bonfils et al. 2013), consistently with $P_{\text{rot}} > 10$ days. We used our recent calibration (Astudillo-Defru et al. in prep.) to compute the R'_{HK} index from S, and from the R'_{HK} vs P_{rot} in the same paper, we estimate $P_{\text{rot}} \simeq 38$ days. The *K2* lightcurve varies with a $< 2 \text{ mmag}$ semi-amplitude and a ~ 40 -day characteristic timescale, consistent with a fairly inactive star and with the estimated P_{rot} . If that photometric variability is entirely due to a dark spot rotating in and out of view, the corresponding RV semi-amplitude is at most $\sim 1.6 \text{ ms}^{-1}$.

In an effort to quantify activity-induced RV variations, we developed new activity metrics. We built an "active" and a "non-active" template from the third of the observed spectra with the highest and the lowest S-indices, respectively, computed two sets of active and non-active RVs, and used their difference $\Delta RV = RV_{\text{act}} - RV_{\text{noact}}$ as an activity tracer. The ΔRV time series (Fig. 1) varies by $\pm 8 \text{ m/s}$ for $\text{BJD} - 2\,450\,000 < 7070$, and is consistent with zero after that date. We surmise that the early large variations result from a spot that not only occults part of the star but also imprints the overall spectrum with its spectral signature. That spot would have been present during the first ~ 25 days of the observations and then disappeared.

We computed our nominal RVs (Sect. 2.2) with a template that includes all spectra regardless of their S index, and it presumably has a sensitivity to activity that is intermediate between that of the active and non-active template. We account for its stellar activity sensitivity by introducing a term proportional to ΔRV in the radial velocity model, with the proportionality coefficient α adjusted as a free parameter in the fit.

3. Analysis

We analyse this multi-planetary system with an n-body dynamical model that describes the gravitational interactions between all components of the system and not just the pull of the central star. Unlike a Keplerian model, the dynamical model therefore accounts for the photometric and radial-velocity changes induced by the mutual attraction of the planets, such as transit timing variations (TTVs), transit duration variations (TDVs), or more generally, transit shape variations. Even though we detect no gravitational interactions, using a dynamical model helps constrain the masses and eccentricities by excluding values for those parameters that would result in detectable interactions or in a highly unstable system.

Our dynamical model uses the well known MERCURY (Chambers 1999) n-body integrator code to compute the three-dimensional position and velocity of all system components as a function of time. The line-of-sight projection of the stellar velocity is compared to the HARPS radial velocities. The sky-projection of the planet-star separations are used, together with the planet-to-star-radius ratios and the limb darkening coefficient, to model the *K2* light curve (Mandel & Agol 2002). We couple the dynamical model with a Monte Carlo Markov Chain (MCMC) code, described in detail in Díaz et al. (2014), to explore the posterior distribution of the parameters. For each MCMC step, we run MERCURY three times with the same model parameters:

- once over the 80 days of the *K2* observations, using the Bulirsch-Stoer algorithm and a 0.02-day timestep to model the light curve with a 1 ppm maximum photometric error
- once over the (disjoint) 103 days of the HARPS observations, again with the Bulirsch-Stoer algorithm and a 0.02 days timestep, to model the radial velocities
- once over a 1000-year interval, using the hybrid symplectic/Bulirsch-Stoer integrator with a 0.5-day timestep (1/20th of the shortest orbital period)

The last run is not compared to any observation but used to ensure the short-term stability of the system, while rejecting any MCMC step where two orbits intersect or where a planet comes within 0.05 au of the star. (Tidal forces are not included in MERCURY.) One would ideally like to evaluate stability on longer time scales, with 1000 years chosen as a compromise between ideality and computational expense.

The physical parameters of the model are the stellar mass and radius, the coefficient of a linear limb-darkening law, the systemic velocity, the planetary masses, the planet-to-star radius ratios, and the planetary orbital parameters (a , e , i , ω , n , and M ; see Table A.2) at reference time 2 456 812 BJD. To minimise correlations, however, we use a different parametrisation for MCMC jump parameters: orbital period (P), conjunction time of the first transit observed by *K2* (T_0), radial velocity semi-amplitude (K), $\sqrt{e} \cos \omega$, and $\sqrt{e} \sin \omega$. Additionally, we fit a global light curve normalization factor, one multiplicative jitter parameter for each data set and α , the amplitude of the ΔRV term of the radial velocity model (Sec. 2.3).

We use non-informative uniform priors for all MCMC model parameters except the stellar mass and radius, for which we adopt the Gaussian distributions of Crossfield et al. (2015) (we also adopt all parameters in common as the starting point of our chains) and the longitude of the ascending node for which we adopt a Gaussian distributions with $\sigma = 2^\circ$ to enforce the observed physical bias towards coplanarity (Fabrycky et al. 2014). We adopt a non-informative prior for the limb-darkening even though this widens the distributions of several parameters, because limb-darkening models have often been found to be inaccurate when the data quality is high enough to probe them. We ran 48 MCMC chains of 180 000 steps and combined their results as described in Díaz et al. (2014).

4. Results

Table A.2 lists the mode and the 68.3% confidence interval for the system parameters. Figures 1 and A.2 show the radial velocity measurements and the transit light curves, together with their respective models. By fitting a stellar spectral energy distribution to the *K2*-3 photometry (Crossfield et al. 2015, Table 1) as described in Díaz et al. (2014), we obtain a 47.5 ± 6.0 pc distance and $E_{(B-V)} < 0.056$ with 68.3% confidence.

Our results agree with Crossfield et al. (2015) for all parameters in common. In addition to adding the radial velocity information, our analysis differs in that we neither impose a circular orbit nor use informative priors on R_*/a or the limb darkening coefficient. We also model the transits of all three planets jointly rather than one planet at a time, enforcing consistency in the derived stellar properties. Our

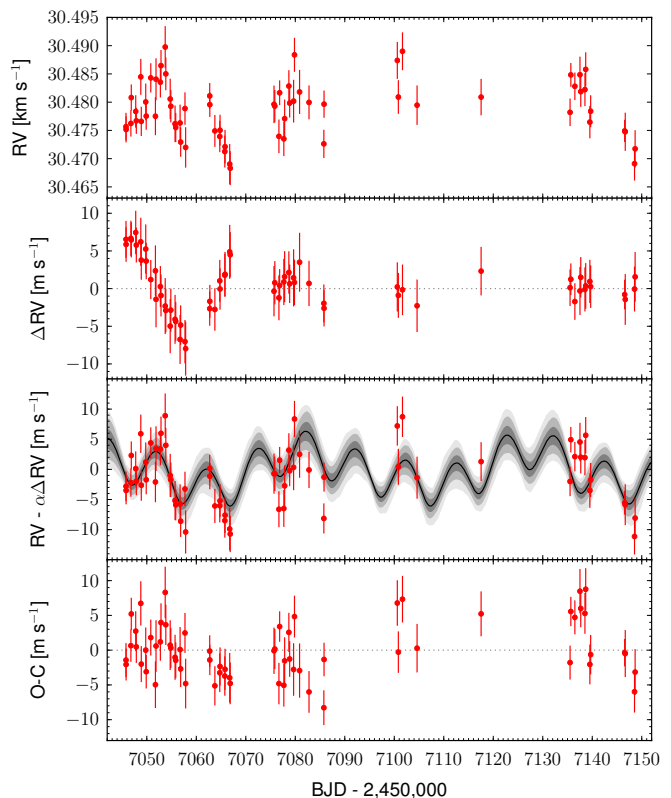


Fig. 1. Time series for, from top to bottom: a) the HARPS radial velocities of K2-3, b) ΔRV (Sec. 2.3), c) the RVs corrected from the $\alpha\Delta RV$ of the maximum likelihood model together with the dynamical model (the solid black line represents the median model, and the shades of grey represent the 68.3, 95.5, and 99.7% Bayesian confidence intervals), and d) the RV residual from the maximum likelihood dynamical model.

approach measures the stellar density more accurately than can be inferred from the average spectrum.

The times of the individual transit are measured with standard errors (which roughly translate to a 1σ detection limits for TTVs) of 1.4, 2.8, and 2.9 minutes for planets *b*, *c*, and *d*, respectively. Over the short time span of the HARPS observations, the radial velocity of the dynamical model differs from that of a three-Keplerian model by at most 27 cm s^{-1} , which is well below the $\sim 2 \text{ m s}^{-1}$ measurement noise.

Owing to the low eccentricities and almost edge-on inclinations, all three planets almost certainly undergo secondary eclipses. Table A.2 lists the epochs and durations of these secondary eclipses.

To evaluate the robustness of our mass measurements, we extended the radial velocity by adding a linear drift, a fourth planet, a term proportional to the bisector of the spectra, and any combination of them. We also experimented with restricting the analysis to those radial velocities that seem unaffected by stellar activity ($\text{BJD} - 2\,450\,000 > 7070$). They always produced similar velocity amplitudes (and masses) for Planet *b*, but a wide range of values for Planets *c* and *d*. We conclude that our data robustly measure the mass of Planet *b*, $8.4 \pm 2.1 M_\oplus$, but not those of *c* and *d*. Many more observations and very careful analysis will be needed to disentangle signatures of

Planets *c* and *d* from the activity signal. Figure 2 shows the RV signal from Planet *b* after removing the other terms of the model.

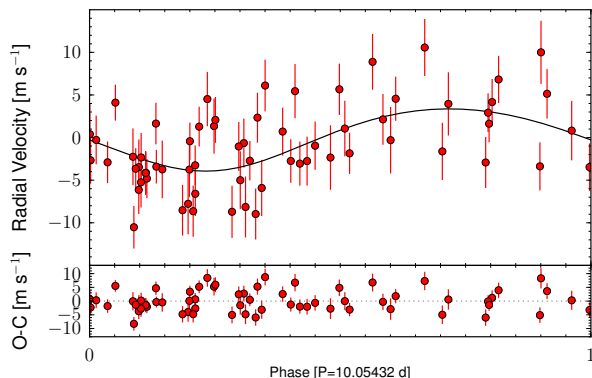


Fig. 2. HARPS radial velocities of K2-3 phased to the period of Planet *b*, with the Keplerian model (solid black line) overlaid, after removal of the Keplerians signals from Planets *c* and *b* and of $\alpha\Delta RV$ activity term of the maximum likelihood model.

When included in the model, the fourth planet converges to a $P_e \sim 100$ -day period and absorbs part of the residuals seen in Fig. 1 (bottom). Model comparison favours the four-planet model only marginally over the simpler three-planet model, with the Bayesian evidence estimators of Perrakis et al. (2014) and Chib & Jeliazkov (2001) giving odd ratios of 4.6 ± 0.3 and 4.9 ± 2.1 , respectively, in favour of the four-planet model. More data will thus be needed to firmly establish whether additional planets orbit K2-3.

Figure 3 adds Planet *b* to the mass-radius diagram of the known small transiting planets. Planet *b* must contain rock with at most a 50% water envelope.

Planets around M stars are ideal for characterisation follow-up, thanks to the favourable planet-to-star surface ratio. The other known low-mass planets transiting bright M stars have a gas envelope (GJ436b and GJ3470b, Butler et al. 2004; Bonfils et al. 2012) or may even potentially consist of 100% water (GJ1214b, Charbonneau et al. 2009). Our measurement of the density of Planet *b* shows that it is

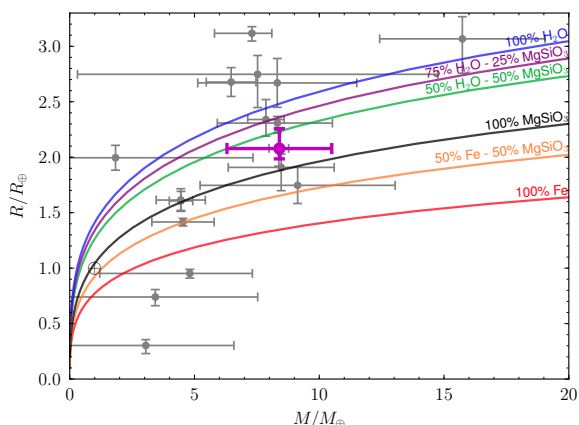


Fig. 3. Radius versus mass diagram of the known small exoplanets (Wright et al. 2011), with planet *b* added (magenta) with 68.3% credible intervals. The colored solid lines represents theoretical models for different compositions (Zeng & Sasselov 2013).

either entirely rocky or mostly rocky with a water envelope. It is the first planet in this category, and the brightness of the star makes it a prime target for follow-up.

Acknowledgements. We thank the ESO La Silla staff for its continuous support, the HARPS observers (C. Mordasini, J. Martins, and A. Sozzetti, as well as L. Kreidberg for her Mandel & Agol code), C. Damiani for discussions of the dynamics of the system, and T. Fenouillet for his assistance with the LAM computing cluster. This paper includes data collected by the *Kepler* mission. Funding for the *Kepler* mission is provided by the NASA Science Mission directorate. Some of the data presented in this paper were obtained from the Mikulski Archive for Space Telescopes (MAST). STScI is operated by the Association of Universities for Research in Astronomy, Inc. under NASA contract NAS5-26555. Support for MAST for non-HST data is provided by the NASA Office of Space Science via grant NNX09AF08G and by other grants and contracts. This research made use of the Exoplanet Orbit Database and the Exoplanet Data Explorer at exoplanets.org. N. A.-D. acknowledges support from CONICYT Becas-Chile number 72120460. XB and JMA acknowledge funding from the European Research Council under the ERC Grant Agreement n. 337591-ExTrA. NCS acknowledges support by Fundação para a Ciência e a Tecnologia (FCT) through Investigador FCT contracts of reference IF/00169/2012, and POPH/FSE (EC) by FEDER funding through the program “Programa Operacional de Factores de Competitividade - COMPETE”. A.S. is supported by the European Union under a Marie Curie Intra-European Fellowship for Career Development with reference FP7-PEOPLE-2013-IEF, number 627202. SCCB and OD thank the CNES for their grants 98761 and 124378, respectively.

References

- Anglada-Escudé, G. & Butler, R. P. 2012, *ApJS*, 200, 15
 Astudillo-Defru, N., Bonfils, X., Delfosse, X., et al. 2014, *ArXiv e-prints* [[arXiv:1411.7048](#)]
 Barros, S. C. C., Almenara, J. M., Deleuil, M., et al. 2014, *A&A*, 569, A74
 Bonfils, X., Delfosse, X., Udry, S., et al. 2013, *A&A*, 549, A109
 Bonfils, X., Gillon, M., Udry, S., et al. 2012, *A&A*, 546, A27
 Butler, R. P., Vogt, S. S., Marcy, G. W., et al. 2004, *ApJ*, 617, 580
 Chambers, J. E. 1999, *MNRAS*, 304, 793
 Charbonneau, D., Berta, Z. K., Irwin, J., et al. 2009, *Nature*, 462, 891
 Chib, S. & Jeliazkov, I. 2001, *Journal of the American Statistical Association*, 96, 270
 Crossfield, I. J. M., Petigura, E., Schlieder, J., et al. 2015, *ArXiv e-prints* [[arXiv:1501.03798](#)]
 Díaz, R. F., Almenara, J. M., Santerne, A., et al. 2014, *MNRAS*, 441, 983
 Fabrycky, D. C., Lissauer, J. J., Ragozzine, D., et al. 2014, *ApJ*, 790, 146
 Howell, S. B., Sobeck, C., Haas, M., et al. 2014, *PASP*, 126, 398
 Lovis, C. & Pepe, F. 2007, *A&A*, 468, 1115
 Mandel, K. & Agol, E. 2002, *ApJ*, 580, L171
 Mayor, M., Pepe, F., Queloz, D., et al. 2003, *The Messenger*, 114, 20
 Perrakis, K., Ntzufras, I., & Tsionas, E. G. 2014, *Computational Statistics & Data Analysis*, 77, 54
 Stone, R. C. 1989, *AJ*, 97, 1227
 Vanderburg, A. 2014, *ArXiv e-prints* [[arXiv:1412.1827](#)]
 Vanderburg, A. & Johnson, J. A. 2014, *PASP*, 126, 948
 Vaughan, A. H., Preston, G. W., & Wilson, O. C. 1978, *PASP*, 90, 267
 Wright, J. T., Fakhouri, O., Marcy, G. W., et al. 2011, *PASP*, 123, 412
 Zeng, L. & Sasselov, D. 2013, *PASP*, 125, 227
 Zucker, S. & Mazeh, T. 2006, *MNRAS*, 371, 1513

Appendix A: Additional figures and tables

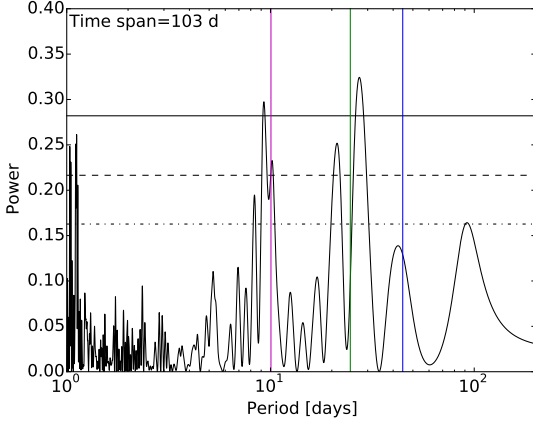


Fig. A.1. Periodogram of HARPS radial velocities of K2-3. The horizontal lines correspond to 1, 2, and 3σ confidence intervals. The false alarm probabilities (FAP) of the main peaks are 0.044% (20-30 days) and 0.0015% (8-10 days). The vertical lines indicate the period of Planets *b*, *c*, and *d* (from left to right).

Table A.1. HARPS radial velocity measurements of K2-3.

BJD - 2 400 000	RV [km s ⁻¹]	$\pm 1\sigma^{\dagger}$ [km s ⁻¹]	ΔRV [m s ⁻¹]	S-index
57045.795776	30.4757	0.0024	6.5	0.769
57045.816981	30.4752	0.0023	5.9	0.724
57046.785448	30.4762	0.0023	6.7	0.775
57046.865234	30.4808	0.0023	6.5	0.782
57047.761529	30.4784	0.0029	7.5	0.742
57047.881539	30.4767	0.0023	5.8	0.731
57048.787741	30.4845	0.0032	6.2	0.696
57048.884890	30.4766	0.0026	3.8	0.826
57049.786450	30.4800	0.0033	5.3	0.629
57049.881769	30.4775	0.0024	3.7	0.777
57050.806327	30.4843	0.0026	1.2	0.653
57051.741719	30.4775	0.0034	2.4	0.520
57051.862734	30.4841	0.0037	-1.4	0.779
57052.740065	30.4835	0.0027	0.3	0.659
57052.870155	30.4865	0.0028	-0.9	0.783
57053.720306	30.4898	0.0037	-2.3	0.657
57053.841750	30.4850	0.0029	-2.9	0.670
57054.727180	30.4806	0.0036	-5.0	0.779
57054.854087	30.4793	0.0029	-2.9	0.666
57055.709838	30.4762	0.0032	-4.1	0.660
57055.846433	30.4755	0.0026	-4.4	0.720
57056.724361	30.4763	0.0032	-6.8	0.570
57056.842204	30.4729	0.0026	-4.8	0.739
57057.713776	30.4789	0.0029	-7.0	0.757
57057.849294	30.4720	0.0036	-8.0	0.822
57062.713162	30.4811	0.0023	-2.7	0.889
57062.733973	30.4796	0.0022	-1.7	0.890
57063.753092	30.4749	0.0028	-2.8	0.838
57064.748274	30.4739	0.0028	1.0	0.976
57064.796239	30.4750	0.0027	-0.1	0.865
57065.762656	30.4713	0.0028	1.8	0.874
57065.807820	30.4721	0.0030	1.9	0.896
57066.751931	30.4690	0.0036	4.9	0.781
57066.853522	30.4683	0.0030	4.5	0.943
57075.700364	30.4796	0.0033	-0.4	0.992
57075.864582	30.4793	0.0029	0.8	1.007
57076.694658	30.4740	0.0030	-1.2	0.015
57076.841851	30.4817	0.0022	0.4	0.980
57077.687319	30.4735	0.0031	0.9	1.023
57077.852660	30.4771	0.0034	1.6	0.015
57078.702537	30.4829	0.0028	2.1	0.950
57078.865482	30.4798	0.0025	0.6	0.918
57079.661385	30.4802	0.0038	1.4	0.015
57079.839990	30.4884	0.0030	0.8	0.014
57080.867369	30.4818	0.0039	3.5	0.015
57082.773669	30.4800	0.0030	0.7	0.939
57085.773295	30.4726	0.0025	-2.0	0.780
57085.810298	30.4797	0.0024	-2.6	0.786
57100.614169	30.4874	0.0033	0.2	0.774
57100.822420	30.4809	0.0030	-0.9	0.822
57101.660042	30.4890	0.0034	-0.2	0.576
57104.607546	30.4795	0.0035	-2.3	0.932
57117.543836	30.4809	0.0032	2.3	0.545
57135.517340	30.4782	0.0024	0.1	0.838
57135.673963	30.4848	0.0021	1.2	0.959
57136.486899	30.4828	0.0024	-1.7	0.742
57137.518119	30.4849	0.0032	-0.3	0.866
57137.679348	30.4819	0.0027	1.5	0.659
57138.523321	30.4822	0.0029	-0.1	0.867
57138.676714	30.4858	0.0030	0.4	0.839
57139.518338	30.4765	0.0029	1.0	0.835
57139.679473	30.4784	0.0028	0.3	0.813
57146.549907	30.4749	0.0020	-0.8	0.825
57146.668220	30.4745	0.0034	-1.4	0.687
57148.541552	30.4691	0.0030	-0.1	0.946
57148.662503	30.4717	0.0033	1.6	0.619

Notes. ^(†) include a systematic error of 60 cm s⁻¹ (Bonfils et al. 2013).

Table A.2. Model parameters. Posterior mode and 68.3% credible intervals. The orbital elements have their origin at the star (*Asteroidal parameters* in the MERCURY code) and are osculating elements for reference time $t_{\text{ref}} = 2\,456\,812$ BJD. We have low confidence in the mass and density of planets *c* and *d* (Sec. 4).

Parameter	Mode and 68.3% credible interval		
Stellar mass, M_\star [M_\odot] [•]	0.612 ± 0.086		
Stellar radius, R_\star [R_\odot] [•]	0.553 ± 0.041		
Stellar density, ρ_\star [ρ_\odot]	3.58 ± 0.61		
Surface gravity, $\log g$ [cgs]	4.734 ± 0.062		
Linear limb darkening coefficient, u [•]	0.573 ± 0.088		
Systemic velocity, γ_0 [km s ^{−1}] [•]	30.48024 ± 0.00063		
	<i>Planet b</i>	<i>Planet c</i>	<i>Planet d</i>
Semi-major axis, a [AU]	0.0775 ± 0.0039	0.1405 ± 0.0067	0.2086 ± 0.010
Eccentricity, e	$[0, 0.12]^* < 0.29^\ddagger$	$[0, 0.08]^* < 0.20^\ddagger$	$[0, 0.09]^* < 0.19^\ddagger$
Inclination, i [°] [†]	$89.59^{+0.24}_{-0.40}$	89.70 ± 0.20	89.79 ± 0.15
Argument of pericentre, ω [°]	180 ± 70	89 ± 110	351 ± 66
Longitude of the ascending node, n [°] [•]	180 (fixed)	180.0 ± 1.8	180.0 ± 1.8
Mean anomaly, M [°]	230 ± 69	21 ± 100	338 ± 67
Period, P [days] [•]	10.05429 ± 0.00022	24.6491 ± 0.0033	44.5705 ± 0.0059
Transit epoch, T_0 [BJD-2,450,000] [•]	6813.41817 ± 0.00082	6812.2784 ± 0.0018	6826.2272 ± 0.0027
Transit duration, T_{14} [hours]	2.563 ± 0.039	3.345 ± 0.079	4.07 ± 0.12
Scaled semi-major axis, a/R_\star	$30.74^{+0.53}_{-2.5}$	$55.90^{+0.97}_{-4.6}$	$82.9^{+1.4}_{-6.9}$
Transit impact parameter, b	$0.21^{+0.21}_{-0.12}$	$0.31^{+0.14}_{-0.21}$	$0.359^{+0.089}_{-0.27}$
Secondary eclipse impact parameter, b_{SE}	$0.310^{+0.079}_{-0.21}$	$0.33^{+0.11}_{-0.22}$	$0.30^{+0.14}_{-0.20}$
Secondary eclipse epoch, T_{SE} [BJD-2,450,000]	$6818.407^{+0.066}_{-0.79}$	6824.59 ± 0.85	$6848.72^{+2.9}_{-0.24}$
Secondary eclipse duration [hours]	2.55 ± 0.25	$3.37^{+0.40}_{-0.17}$	$4.01^{+0.41}_{-0.21}$
Radial velocity semi-amplitude, K [m s ^{−1}] [•]	3.60 ± 0.87	$0.61^{+0.66}_{-0.37}$	2.84 ± 0.90
Radius ratio, R_p/R_\star [•]	0.03477 ± 0.00064	0.02770 ± 0.00070	0.02495 ± 0.00074
$\sqrt{e} \cos \omega$ [•]	$-0.283^{+0.33}_{-0.065}$	0.01 ± 0.19	$0.263^{+0.052}_{-0.28}$
$\sqrt{e} \sin \omega$ [•]	$-0.05^{+0.21}_{-0.14}$	$0.128^{+0.10}_{-0.26}$	0.00 ± 0.16
Planet mass, M_p [M_\oplus]	8.4 ± 2.1	$2.1^{+2.1}_{-1.3}$	11.1 ± 3.5
Planet radius, R_p [R_\oplus]	$2.078^{+0.18}_{-0.093}$	$1.644^{+0.16}_{-0.065}$	1.53 ± 0.11
Planet density, ρ_p [g cm ^{−3}]	$4.32^{+2.0}_{-0.76}$	$1.82^{+3.0}_{-0.96}$	17.5 ± 6.3
<i>K2</i> long-cadence multiplicative jitter [•]	1.020 ± 0.049		
HARPS multiplicative jitter [•]	1.43 ± 0.13		
Amplitude of the ΔRV term, α [•]	-0.21 ± 0.19		

Notes. (•) MCMC jump parameter. (†) reflected with respect to $i = 90^\circ$, the supplementary angle is equally probable. (*) 68.3% highest density interval. (‡) upper limit, 99% confidence. $T_0 \equiv t_{\text{ref}} - \frac{P}{2\pi} (M - E + e \sin E)$ with $E = 2 \arctan \left\{ \sqrt{\frac{1-e}{1+e}} \tan \left[\frac{1}{2} \left(\frac{\pi}{2} - \omega \right) \right] \right\}$, $P \equiv \sqrt{\frac{4\pi^2 a^3}{GM_\star}}$, $K \equiv \frac{M_p \sin i}{M_\star^{2/3} \sqrt{1-e^2}} \left(\frac{2\pi G}{P} \right)^{1/3}$. $M_\odot = 1.98842 \times 10^{30}$ kg, $R_\odot = 6.95508 \times 10^8$ m, $M_\oplus = 5.9736 \times 10^{24}$ kg, $R_\oplus = 6,378,137$ m.

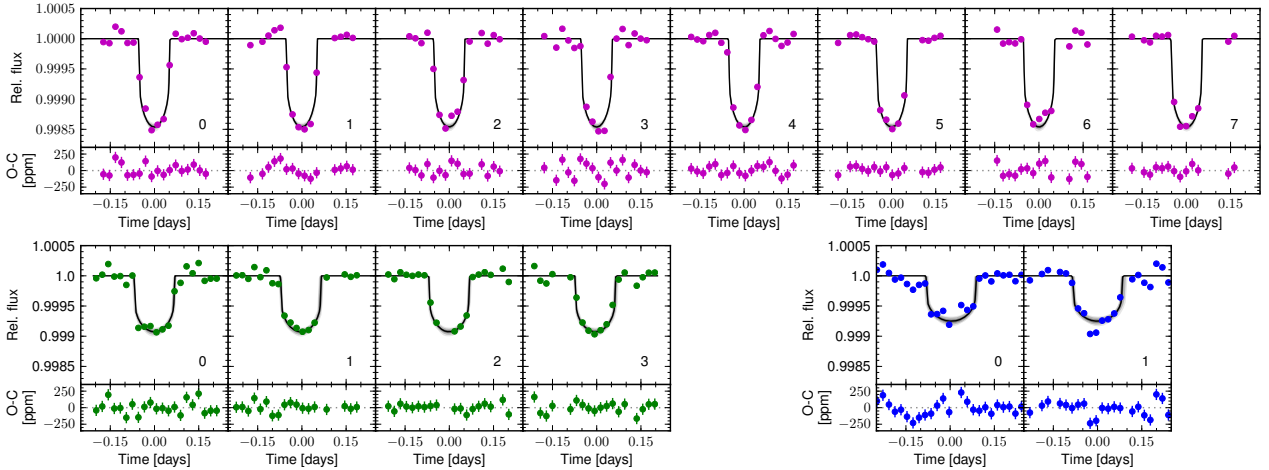


Fig. A.2. As in Figure 1, but for the *K2* photometry of K2-3 (from top to bottom and left to right: planet *b*, planet *c*, and planet *d*). Each transit is centered relative to the linear ephemeris.